

FLUID/STRUCTURE TWIN TAIL BUFFET RESPONSE OVER A WIDE RANGE OF ANGLES OF ATTACK

Osama A. Kandil¹, Essam F. Sheta² and Steven J. Massey³
Aerospace Engineering Department
Old Dominion University, Norfolk, VA 23529, USA

ABSTRACT

The buffet response of the flexible twin-tail/delta wing configuration-a multidisciplinary problem is solved using three sets of equations on a multi-block grid structure. The first set is the unsteady, compressible, Reynolds-averaged Navier-Stokes equations which are used for obtaining the flow-field vector and the aerodynamic loads on the twin tails. The second set is the coupled aeroelastic equations which are used for obtaining the bending and torsional deflections of the twin tails. The third set is the grid-displacement equations which are used for updating the grid coordinates due to the tail deflections. The configuration is pitched at wide range of angles of attack; 15° to 40° , and the freestream Mach number and Reynolds number are 0.3 and 1.25 million, respectively. With the twin tails fixed as rigid surfaces, the problem is solved for the initial flow conditions. Next, the problem is solved for the twin tail response for uncoupled bending and torsional vibrations due to the unsteady loads produced by the vortex breakdown flow of the leading-edge vortex cores. The configuration is investigated for two spanwise positions of the twin tails; inboard and outboard locations. The computational results are validated and are in very good agreement with the experimental data of Washburn, et. al.

INTRODUCTION

In order to maximize the effectiveness of the fighter aircraft that operate well beyond the buffet onset boundary, the design of the new generation of fighter aircraft should account for both high maneuver capabilities at high and wide range of

angles of attack, and the aeroelastic buffet characteristics at high alpha. The maneuver capabilities are achieved, for example in the F/A-18 fighter, through the combination of the leading-edge extension (LEX) with a delta wing and the use of vertical tails. The LEX maintains lift at high angles of attack by generating a pair of vortices that trail aft over the top of the aircraft. The vortex entrains air over the vertical tails to maintain stability of the aircraft. At some flight conditions, the vortices emanating from the highly-swept LEX of the delta wing breakdown before reaching the vertical tails which get bathed in a wake of unsteady highly-turbulent, swirling flow. The vortex-breakdown flow produces unsteady, unbalanced loads on the vertical tails and causes a peak in the pressure spectrum that may be tuned to different structural modes depending on the angle of attack and dynamic pressure. This in turn produce severe buffet on the tails and has led to their premature fatigue failure. Therefore, the evaluation of the buffet characteristics must account for the turbulent characteristics of the oncoming flow. If the power spectrum of the turbulence is accurately predicted, the intensity of the buffeting motion can be computed and the structural components of the aircraft can be designed accordingly.

Experimental investigation of the vertical tail buffet of the F/A-18 models have been conducted by several investigators such as Sellers, et al.¹, Erickson, et al.², Wentz³, Lee and Brown⁴, and Cole, et al.⁵. These experiments showed that the vortex produced by the LEX of the wing breaks down ahead of the vertical tails at angles of attack of 25° and higher producing unsteady loads on the vertical tails, and the buffet

¹Professor, Eminent Scholar and Dept. Chair, Associate Fellow AIAA.

²Ph.D. Graduate Research Assistant, Member AIAA.

³Ph.D. Graduate Research Assistant, Member AIAA.

response occurs in the first bending mode, increases with increasing dynamic pressure and is larger at $M = 0.3$ than that at a higher Mach numbers. Bean and Lee⁶ showed that buffeting in the torsional mode occurred at a lower angle of attack and at larger levels compared to the fundamental bending mode.

An extensive experimental investigation has been conducted to study vortex-tail interaction on a 76° sharp-edged delta wing with vertical twin-tail configuration by Washburn, Jenkins and Ferman⁷. The vertical tails were placed at nine locations behind the wing. The experimental data showed that the aerodynamic loads are more sensitive to the chordwise tail location than its spanwise location. As the tails were moved laterally toward the vortex core, the buffeting response and excitation were reduced. Although the tail location did not affect the vortex core trajectories, it affected the location of vortex-core breakdown. Moreover, the investigation showed that the presence of a flexible tail can affect the unsteady pressures on the rigid tail on the opposite side of the model.

Kandil, Kandil and Massey⁸ presented the first successful computational simulation of the vertical tail buffet using a delta wing-single flexible vertical tail configuration. The tail was allowed to oscillate in bending modes. The flow conditions and wing angle of attack have been selected to produce an unsteady vortex-breakdown flow. Unsteady vortex breakdown of leading-edge vortex cores was captured, and unsteady pressure forces were obtained on the tail. Kandil, et al.^{9–11} allowed the vertical tail to oscillate in both bending and torsional modes. The total deflections and the frequencies of deflections and loads of the coupled bending-torsion case were found to be one order of magnitude higher than those of the bending case only. The loads on the tail in the transonic flow regime were one order of magnitude lower than those of the subsonic flow. Also, it has been shown that the tail oscillations change the vortex breakdown locations and the unsteady aerodynamic loads on the wing and tail.

In recent papers by the present authors^{12,13}, the buffet response of the F/A-18 and a generic F-117 twin tails were considered at $\alpha = 30^\circ$ and for different spanwise locations of the twin tails. A multi-block grid structure was used to solve

the problem. The loads, deflections, frequencies and root bending moments were reduced as the twin tails moved laterally toward the vortex core. The outboard location of the tails produced the least of these responses. The computational results were in full qualitative agreement with the experimental data of Washburn, et al.⁷.

In this paper, we consider the buffet response of delta-wing/twin-tail configuration similar to the one used by Washburn, et. al.⁷. The Baldwin and Lomax two-layer turbulent algebraic model¹⁴ is used to model flow turbulence. A multi-block grid structure is used to solve the problem over a wide range of angles of attack from 15° to 40° , and for two spanwise locations of the twin tails. The computational results are compared with the experimental data of Washburn, et. al.

FORMULATION

The formulation consists of three sets of governing equations along with certain initial and boundary conditions. The first set is the unsteady, compressible, Reynolds-averaged Navier-Stokes equations. The second set consists of the aeroelastic equations for bending and torsional modes. The third set consists of equations for deforming the grid according to the twin tail deflections. Next, the governing equations of each set along with the initial and boundary conditions are given.

Fluid-Flow Equations:

The conservative form of the dimensionless, unsteady, compressible, full Navier-Stokes equations in terms of time-dependent, body-conformed coordinates ξ^1 , ξ^2 and ξ^3 is given by

$$\frac{\partial \bar{Q}}{\partial t} + \frac{\partial \bar{E}_m}{\partial \xi^m} - \frac{\partial (\bar{E}_v)_s}{\partial \xi^s} = 0; m = 1-3, s = 1-3 \quad (1)$$

where

$$\xi^m = \xi^m(x_1, x_2, x_3, t) \quad (2)$$

$$\bar{Q} = \frac{1}{J}[\rho, \rho u_1, \rho u_2, \rho u_3, \rho e]^t, \quad (3)$$

\bar{E}_m and $(\bar{E}_v)_s$ are the ξ^m -inviscid flux and ξ^s -viscous and heat conduction flux, respectively. Details of these fluxes are given in Ref. 8. The

details of the two-layer turbulent algebraic model are given in Ref. 14.

Aeroelastic Equations:

The dimensionless, linearized governing equations for the coupled bending and torsional vibrations of a vertical tail that is treated as a cantilevered beam are considered. The tail bending and torsional deflections occur about an elastic axis that is displaced from the inertial axis. These equations for the bending deflection, w , and the twist angle, θ , are given by

$$\frac{\partial^2}{\partial z^2} \left[EI(z) \frac{\partial^2 w}{\partial z^2}(z, t) \right] + m(z) \frac{\partial^2 w}{\partial t^2}(z, t) + m(z) x_\theta(z) \frac{\partial^2 \theta}{\partial t^2}(z, t) = N(z, t) \quad (4)$$

$$\frac{\partial}{\partial z} \left[GJ(z) \frac{\partial \theta}{\partial z} \right] - m(z) x_\theta(z) \frac{\partial^2 w}{\partial t^2}(z, t) - I_\theta(z) \frac{\partial^2 \theta}{\partial t^2}(z, t) = -M_t(z, t) \quad (5)$$

where z is the vertical distance from the fixed support along the tail length, l_t , EI and GJ the bending and torsional stiffness of the tail section, m the mass per unit length, I_θ the mass-moment of inertia per unit length about the elastic axis, x_θ the distance between the elastic axis and inertia axis, N the normal force per unit length and M_t the twisting moment per unit length. The characteristic parameters for the dimensionless equations are c^* , a_∞^* , ρ_∞^* and c^*/a_∞^* for the length, speed, density and time; where c^* is the delta wing root-chord length, a_∞^* the freestream speed of sound and ρ_∞^* the freestream air density. The geometrical and natural boundary conditions on w and θ are given by

$$\begin{aligned} w(0, t) &= \frac{\partial w}{\partial z}(0, t) = \frac{\partial^2 w}{\partial z^2}(l_t, t) \\ &= \frac{\partial}{\partial z} \left[EI(l_t) \frac{\partial^2 w}{\partial z^2}(l_t, t) \right] = 0 \end{aligned} \quad (6)$$

$$\theta(0, t) = \frac{\partial \theta}{\partial z}(l_t, t) = 0 \quad (7)$$

The solution of Eqs. (4) and (5) are given by

$$w(z, t) = \sum_{i=1}^{\hat{I}} \phi_i(z) q_i(t) \quad (8)$$

$$\theta(z, t) = \sum_{j=\hat{I}+1}^M \phi_j(z) q_j(t) \quad (9)$$

where ϕ_i and ϕ_j are comparison functions satisfying the free-vibration modes of bending and torsion, respectively, and q_i and q_j are generalized coordinates for bending and torsion, respectively. In this paper, the number of bending modes, \hat{I} , is six and the number of torsion modes, $M - \hat{I}$, is also six. Substituting Eqs. (8) and (9) into Eqs. (4) and (5) and using the Galerkin method along with integration by parts and the boundary conditions, Eqs (6) and (7), we get the following equation for the generalized coordinates q_i and q_j in matrix form:

$$\begin{bmatrix} M_{11} & M_{12} \\ M_{21} & M_{22} \end{bmatrix} \begin{pmatrix} \ddot{q}_i \\ \ddot{q}_j \end{pmatrix} + \begin{bmatrix} K_{11} & 0 \\ 0 & K_{22} \end{bmatrix} \begin{pmatrix} q_i \\ q_j \end{pmatrix} = \begin{pmatrix} \hat{N}_1 \\ \hat{N}_2 \end{pmatrix} \quad ; i = 1, 2, \dots, \hat{I} \quad ; j = \hat{I} + 1, \dots, M \quad (10)$$

where

$$\begin{aligned} M_{11} &= \int_0^{l_t} m \phi_r \phi_i dz \\ M_{12} &= M_{21} = \int_0^{l_t} m x_\theta \phi_r \phi_j dz \\ M_{22} &= \int_0^{l_t} I_\theta \phi_s \phi_j dz \end{aligned} \quad (11)$$

$$\begin{aligned} K_{11} &= \int_0^{l_t} EI \frac{d^2 \phi_r}{dz^2} \frac{d^2 \phi_i}{dz^2} dz \\ K_{22} &= \int_0^{l_t} GJ \frac{d \phi_s}{dz} \frac{d \phi_j}{dz} dz \end{aligned} \quad (12)$$

$$\begin{aligned} \hat{N}_1 &= \int_0^{l_t} \phi_r N dz \\ \hat{N}_2 &= \int_0^{l_t} \phi_s M_t dz \end{aligned} \quad (13)$$

Similar aeroelastic equations were developed for sonic analysis of wing flutter by Strganac¹⁵. The numerical integration of Eqs. (11)-(13) is obtained using the trapezoidal method with 125 points to improve the accuracy of integrations. The solution of Eq. (10), for $q_i; i = 1, 2, \dots, \hat{I}$, and $q_j; j = \hat{I} + 1, \dots, M$, is obtained using the Runge-Kutta scheme. Next, w , and θ are obtained from Eqs. (8) and (9).

Grid Displacement Equations:

Once w and θ are obtained at the $n + 1$ time step, the new grid coordinates are obtained using simple interpolation equations. In these equations, the twin tail bending displacements, $w_{i,j,k}^{n+1}$, and their displacement through the torsion angle, $\theta_{i,j,k}^{n+1}$ are interpolated through cosine functions.

Boundary and Initial Conditions:

Boundary conditions consist of conditions for the fluid flow and conditions for the aeroelastic bending and torsional deflections of the twin tail. For the fluid flow, the Riemann-invariant boundary conditions are enforced at the inflow and outflow boundaries of the computational domain. At the plane of geometric symmetry, periodic boundary conditions are specified with the exception of grid points on the tail. On the wing surface, the no-slip and no-penetration conditions are enforced and $\frac{\partial p}{\partial n} = 0$. On the tail surface, the no-slip and no-penetration conditions for the relative velocity components are enforced (points on the tail surface are moving). The normal pressure gradient is no longer equal to zero due to the acceleration of the grid points on the tail surface. This equation becomes $\frac{\partial p}{\partial n} = -\rho \bar{a}_t \cdot \hat{n}$, where \bar{a}_t is the acceleration of a point on the tail and \hat{n} is the unit normal.

Initial conditions consist of conditions for the fluid flow and conditions for the aeroelastic deflections of the twin tail. For the fluid flow, the initial conditions correspond to the freestream conditions with no-slip and no-penetration conditions on the wing and tail. For the aeroelastic deflections of the tail, the initial conditions for any point on the tail are that the displacement and velocity are zero, $w(z, 0) = 0$, $\frac{\partial w}{\partial t}(z, 0) = 0$, $\theta(z, 0) = 0$ and $\frac{\partial \theta}{\partial t}(z, 0) = 0$.

METHOD OF SOLUTION

The first step is to solve for the fluid flow problem using the vortex-breakdown conditions and keeping the tail as a rigid beam. Navier-Stokes equations are solved using the implicit, flux-difference splitting finite-volume scheme. The grid speed $\frac{\partial \xi^m}{\partial t}$ is set equal to zero in this step. This step provides the flow field solution along with the pressure differences across the tails. The pressure differences are used to generate the normal force and twisting moment per unit length of each tail. Next, the aeroelastic equations are used to obtain the twin tail deflections, $w_{i,j,k}$ and $\theta_{i,j,k}$. The grid displacement equations are then used to compute the new grid coordinates. The metric coefficient of the coordinate Jacobian matrix are updated as well as the grid speed, $\frac{\partial \xi^m}{\partial t}$. This computational cycle is repeated every time step.

COMPUTATIONAL APPLICATIONS AND DISCUSSION

Twin Tail-Delta Wing Configuration:

The twin tail-delta wing configuration consists of a 76° -swept back, sharp-edged delta wing (aspect ratio of one) and dynamically scaled flexible twin tails similar to those used by Washburn, et. al.⁷. The vertical tails are oriented normal to the upper surface of the delta wing and have a centerline sweep of 53.5° . A multi-block grid consisting of 4 blocks is used for the solution of the problem. The first block is a O-H grid for the wing and upstream region, with $101 \times 50 \times 54$ grid points in the wrap around, normal and axial directions, respectively. The second block is a H-H grid for the inboard region of the twin tails, with $23 \times 50 \times 13$ grid points in the wrap around, normal and axial directions, respectively. The third block is a H-H grid for the outboard region of the twin tails, with $79 \times 50 \times 13$ grid points in the wrap around, normal and axial directions, respectively. The fourth block is a O-H grid for the downstream region of the twin tails, with $101 \times 50 \times 25$ grid points in the wrap around, normal and axial directions, respectively. Figure 1 shows the grid topology and a front view blow-up of the twin tail-delta wing configuration.

Each tail is made of a single Aluminum spar and Balsa wood covering. The Aluminum spar has a taper ratio of 0.3 and a constant thickness of 0.001736. The chord length at the root is 0.03889 and at the tip is 0.011667, with a span length of 0.2223. The Aluminum spar is constructed from 6061-T6 alloy with density, ρ , moduli of elasticity and rigidity, E and G, of 2693 kg/m^3 , $6.896 \times 10^{10} \text{ N/m}^2$ and $2.5925 \times 10^{10} \text{ N/m}^2$; respectively. The corresponding dimensionless quantities are 2198, 4.595×10^5 and 1.727×10^5 ; respectively.

The Balsa wood covering has a taper ratio of 0.23 and aspect ratio of 1.4. The chord length at the root is 0.2527 and at the tip is 0.058, with a span length of 0.2223. The Balsa thickness decreases gradually from 0.0211 at the tail root to 0.0111 at the tail midspan and then constant thickness of 0.0111 is maintained to the tail tip. The tail cross section is a semi-diamond shape with bevel angle of 20° . The Balsa density, moduli of elasticity and rigidity, E and G, are 179.7 kg/m^3 , $6.896 \times 10^8 \text{ N/m}^2$ and

$2.5925 \times 10^8 \text{ N/m}^2$; respectively. The corresponding dimensionless quantities are 147, 4.595×10^3 and 1.727×10^3 ; respectively. Figure 2 shows a schematic of the tail used in this study. The tails are assumed to be magnetically suspended and the leading edge of the tail root is positioned at $x/c = 1.0$, measured from the wing apex. The configuration is pitched at a wide range of angles of attack 15° to 40° , and the freestream Mach number and Reynolds number are 0.3 and 1.25×10^6 ; respectively.

The configuration is investigated for two spanwise positions of the twin tails; the inboard location and the outboard location corresponding to a separation distance between the twin tails of 33% and 78% of the wing span; respectively.

RESULTS AND DISCUSSION

Parametric Study:

Figure 3 shows the effect of the spanwise tail location on the configuration lift coefficient as a function of angle of attack. The lift coefficient is almost insensitive to the spanwise tail location. The figure also shows a very close agreement with the experimental results. Figures 4a and 4b show the mean root bending moments and the RMS root bending moments as a function of angle of attack, respectively. Positive moments correspond to an outward force on the tails. The mean value of the moment increases with the angle of attack and then reduces at high angles. The RMS value of the moment also increases with the angle of attack. The buffet loads in terms of the root bending moment are greatest with the tails in the inboard position; almost throughout the whole range of angle of attack. The agreement with the experimental data is good. The discrepancies in the results are attributed to the fact that the structural model of the tail is not fully identical to the experimental model. The additional Ballast weights in the tails of the experimental model is not modeled, and Washburn in his experimental work used one flexible tail and one rigid tail while we are using two flexible tails. In the experimental work, the presence of a flexible tail was found to affect the loads and pressures on the other rigid tail.

Figure 5 shows the normalized RMS of the surface pressures (p/q_∞) on the inner and outer

surfaces of the inboard tails at the specified five locations shown in Fig. 2. The experimental results of Washburn⁷ are also shown. The RMS surface pressures in all locations increases with the increase of angle of attack, where the vortex breakdown moves upstream of the tails. The outer surface of the tails experience larger RMS pressure levels than those of the inner surface. On the inner surface, the nearly tip point (location 1) experiences larger pressure levels than the nearly root point (location 5). On the outer surface, the nearly root point experiences larger pressure levels than those of the nearly tip point. Figure 6 shows the normalized RMS of the surface pressures on the inner and outer surfaces of the outboard tails at the specified five locations. The observations are similar to the case of inboard tails, except that the inner surface RMS pressure levels are larger than those of the outer surface levels of the outboard tail case. The inboard tails experience larger pressure levels than those of the outboard tails. These results are in good qualitative agreement with the experimental data. The discrepancies between the two results are, again, attributed to the reasons stated before.

Detailed Results at $\alpha = 25^\circ$:

Figures 7 and 8 show front views for the total pressure contours on the wing surface and in cross flow planes at $x = 1.03$ and $x = 1.22$, and the instantaneous streamlines of the inboard tail position. The vortex cores are almost symmetric at both locations, and they are totally outboard of the twin tail. The cores are moved upward as the flow traveled downstream. Smaller size vortex cores appear underneath the primary wing vortex and it becomes larger in size as it travels downstream. These are the tail vortices observed by Washburn⁷. The tail vortices exist at the outer surfaces of the tails and they are rotating in the opposite direction to those of the primary wing vortices. Figure 9 shows the distribution of the total structural deflection and the root bending moment for the left and right tails. The tails deflections are in first, second and third mode shapes. Both deflections and root bending moment increase rapidly and reach periodic response around $t^* = 20$.

Figures 10 and 11 show front views for the total pressure contours on the wing surface and in cross flow planes at $x = 1.03$ and $x = 1.22$, and the instantaneous streamlines of the outboard tail

position. The tails cut through the vortex breakdown flow of the leading-edge vortex cores. The flow is almost symmetric. The tail vortices are also outboard of the tails but larger in size than those of the inboard tails case. The location of the vortex core with respect to the tail produces an increase in the aerodynamic damping, causing the tail deflection to decrease. The tail vortices are also shown to rotate in the opposite direction to those of the primary wing vortices. Figure 12 shows the distribution of the total structural deflection and the root bending moment for the left and right tails. The levels of deflection are lower than those of the inboard tails position. The frequency of the root bending moment is higher than that of the inboard tail case, and the deflections seem to be damped and stable at this angle of attack. Figure 13 shows the distribution of the surface pressure coefficient covering the wing from $x = 0.3$ to $x = 1.0$. Typical turbulent flow distribution are observed, where the largest suction peaks are pronounced at the position of the wing vortex cores. It is obvious that the vortex breakdown does not occur over the wing surface at this angle of attack.

Detailed results at $\alpha = 40^\circ$:

Figures 14 and 15 show front views for the total pressure contours on the wing surface and in cross flow planes at $x = 1.03$ and $x = 1.22$, and the instantaneous streamlines for the inboard tail position. The primary leading-edge vortex cores experience a breakdown at about $x = 0.28$, and the vortex breakdown flow becomes large in size, and partially covers the region inboard the twin tails. The vertical position of the vortex cores is higher than that at $\alpha = 25^\circ$, and it moves upward as the flow travels downstream. The tail vortices are more distinct than those of $\alpha = 25^\circ$. Figure 16 shows the distribution of the total structural deflection and the root bending moment for the left and right tails. The two tails are deflected in one direction only in first, second and third mode shapes. The frequency of the root bending moment is lower than that of the case of $\alpha = 25^\circ$. Periodic responses have not been reached within the computational time covered.

Figures 17 and 18 show front views for the total pressure contours on the wing surface and in cross flow planes at $x = 1.03$ and $x = 1.22$, and the instantaneous streamlines for the outboard

tail position. The tails cut through the vortex breakdown flow of the leading-edge vortex cores, and the breakdown is larger in size than that of the case of $\alpha = 25^\circ$. The vortex cores are moved more upward than that of the case of $\alpha = 25^\circ$ and continue moving upward as the flow travels downstream. Also, the tail vortex is larger in size than that of the $\alpha = 25^\circ$ case. This also would increase the aerodynamic damping on the tails. The vortex breakdown flow is almost symmetric. Figure 19 shows the distribution of the total structural deflection and the root bending moment for the left and right tails. The two tails are deflected in one direction only in first and second mode shapes. The frequency of deflection is the same as that of the inboard tail case but lower than that of the case of $\alpha = 25^\circ$. The load levels are two order of magnitude higher than those of the case of $\alpha = 25^\circ$. Figure 20 shows the distribution of the surface pressure coefficient covering the wing from $x = 0.3$ to $x = 1.0$. Suction peaks observed over the wing are higher than those of the case of $\alpha = 25^\circ$. It is indicated from the distribution that vortex breakdown covers most of the wing. After 9,600 time steps, the distribution changed completely due to the upstream effect of the tail deflections, and the vortex breakdown covers the whole wing.

Figures 21 and 22 show the tail surface flow on the inner and outer surfaces of the outboard tails, respectively, for $\alpha = 20^\circ, 30^\circ$ and 40° . The flow separation line is shown to start from the leading edge of the root to the middle of the tail tip. The separation line moves downstream as the angle of attack increases. The tail vortex attachment line is observed on the outer surface of the tail near and parallel to the tail root and along the tail root. This is more clear at higher angles of attack, $\alpha = 30^\circ$ and 40° . These results are in complete agreement with the experimental data of Washburn⁷.

CONCLUDING REMARKS

The computational results of the FTNS3D code of the present paper and the experimental data of Washburn, et. al. are in very good agreement. The buffeting levels increase as the angle of attack increases. The case of inboard tails at $\alpha = 25^\circ$ produces the largest buffet loads and deflections. In general, the inboard location of the twin tails produces the largest bending-torsion

loads, deflections, frequencies and root bending moments when compared with the midspan and outboard locations. The frequencies of the loads and deflections of the tails decrease as the angle of attack increases.

ACKNOWLEDGMENT

This research work is supported under Grants No. NAG-1-994 and NAG-1-648 by the NASA Langley Research Center. The authors would like to recognize the computational resources provided by the NAS facilities at Ames Research Center and the NASA Langley Research Center.

REFERENCES

1. Sellers, W. L. III, Meyers, J. F. and Hepner, T. E., "LDV Survey Over a Fighter Model at Moderate to High Angle of Attack," SAE Paper 88-1448, 1988.
2. Erickson, G. E., Hall, R. M., Banks, D. W., Del Frate, J. H., Shreiner, J. A., Hanley, R. J. and Pulley, C. T., "Experimental Investigation of the F/A-18 Vortex Flows at Subsonic Through Transonic Speeds," AIAA 89-2222, 1989.
3. Wentz, W. H., "Vortex-Fin Interaction on a Fighter Aircraft," AIAA 87-2474, AIAA Fifth Applied Aerodynamics Conference, Monterey, CA August 1987.
4. Lee, B. and Brown, D., "Wind Tunnel Studies of F/A-18 Tail Buffet," AIAA 90-1432, 1990.
5. Cole, S. R., Moss, S. W. and Dogget, R. V., Jr., "Some Buffet Response Characteristics of a Twin-Vertical-Tail Configuration," NASA TM-102749, October 1990.
6. Bean, D. E. and Lee, B. H. K., "Correlation of Wind Tunnel and Flight Test Data for F/A-18 Vertical Tail Buffet," AIAA 94-1800-CP, 1994.
7. Washburn, A. E., Jenkins, L. N. and Ferman, M. A., "Experimental Investigation of Vortex-Fin Interaction," AIAA 93-0050, AIAA 31st ASM, Reno, NV, January 1993.
8. Kandil, O. A., Kandil, H. A. and Massey, S. J., "Simulation of Tail Buffet Using Delta Wing-Vertical Tail Configuration," AIAA 93-3688-CP, AIAA Atmospheric Flight Mechanics Conference, Monterey, CA August 1993, pp. 566-577.
9. Kandil, O. A., Massey, S. J., and Kandil, H. A., "Computations of Vortex-Breakdown Induced Tail Buffet Undergoing Bending and Torsional Vibrations," AIAA 94-1428-CP, AIAA/ASME/ASCE/ASC Structural, Structural Dynamics and Material Conference, SC April 1994, pp. 977-993.
10. Kandil, O. A., Massey, S. J. and Sheta, E. F., "Structural Dynamics/CFD Interaction for Computation of Vertical Tail Buffet," International Forum on Aeroelasticity and Structural Dynamics, Royal Aeronautical Society, Manchester, U.K., June 26-28, 1995, pp. 52.1-52.14. Also published in Royal Aeronautical Journal, August/September 1996, pp. 297-303.
11. Kandil, O. A., Sheta, E. F. and Massey, S. J., "Buffet Responses of a Vertical Tail in Vortex Breakdown Flows," AIAA 95-3464-CP, AIAA Atmospheric Flight Mechanics Conference, Baltimore, MD, August 7-9, 1995, pp. 345-360.
12. Kandil, O. A., Sheta, E. F. and Massey, S. J., "Twin Tail/Delta Wing Configuration Buffet Due to Unsteady Vortex Breakdown Flow," AIAA 96-2517-CP, 14th AIAA Applied Aerodynamics Conference, New Orleans, LA, June 18-20, 1996, pp. 1136-1150.
13. Kandil, O. A., Massey, S. J. and Sheta, E. F., "Aerostructural Vortical Flow Interactions With Applications to F/A-18 and F-117 Tail Buffet," High-Angle-of-Attack Technology Conference, NASA Langley Research Center, Hampton, VA, September 17-19, 1996.
14. Baldwin, B. and Lomax, H., "Thin-Layer Approximation and Algebraic Model for Separated Turbulent Flows," AIAA Paper 78-0257, January, 1978.
15. Straganac, T. W., "A Numerical Model of Unsteady, Subsonic Aeroelastic Behavior," NASA Technical Memorandum 100487, December 1987.

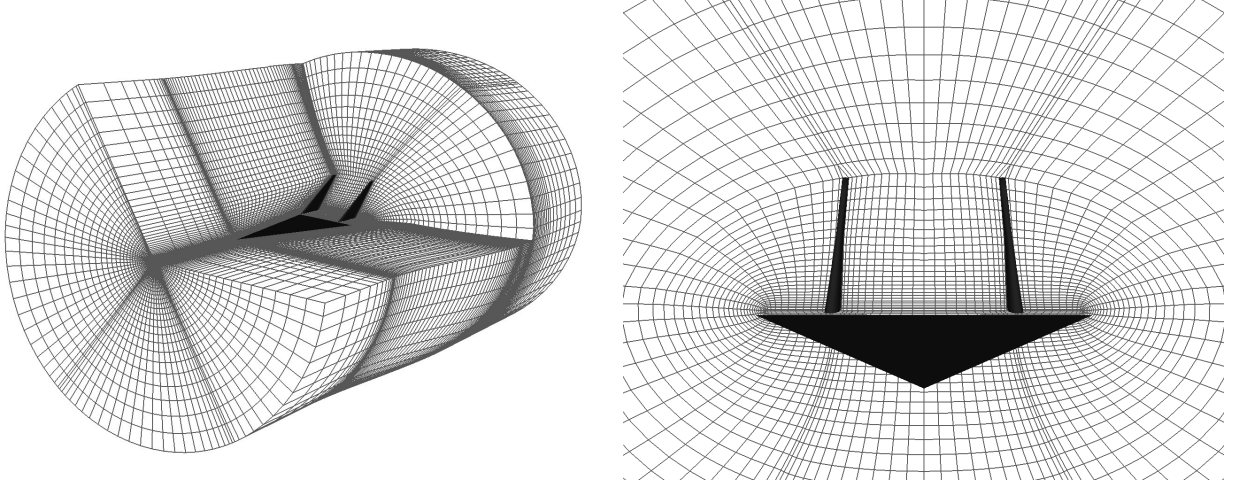


Figure 1: Three-dimensional grid topology and blow-up of the twin tail-delta wing configuration (the tails are in midspan position).

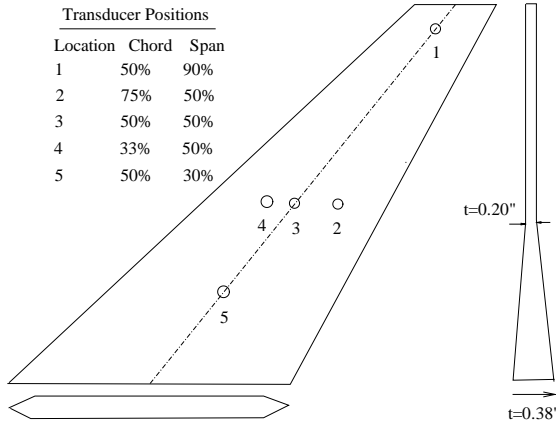


Figure 2: Schematic of the tail

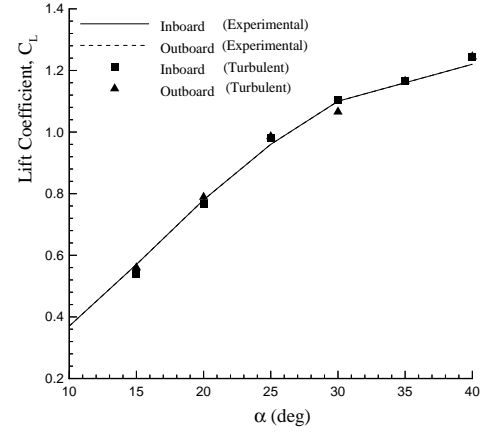
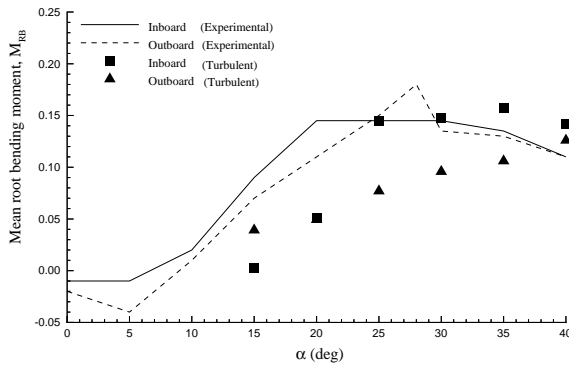
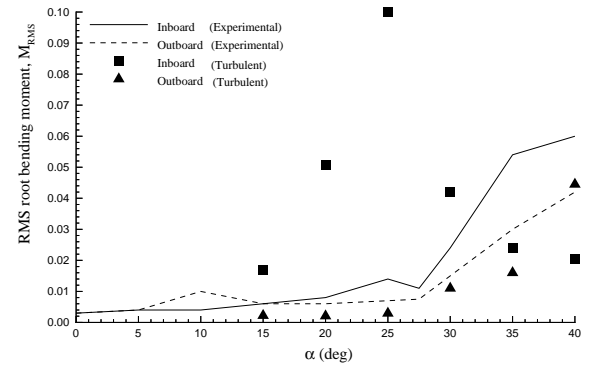


Figure 3: Effect of spanwise tail location on the lift coefficient curve.

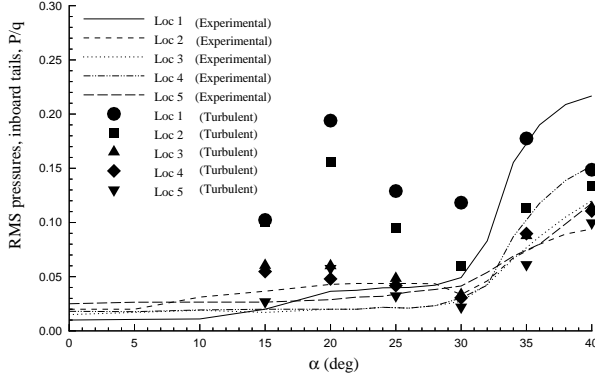


(a) Mean root bending moment

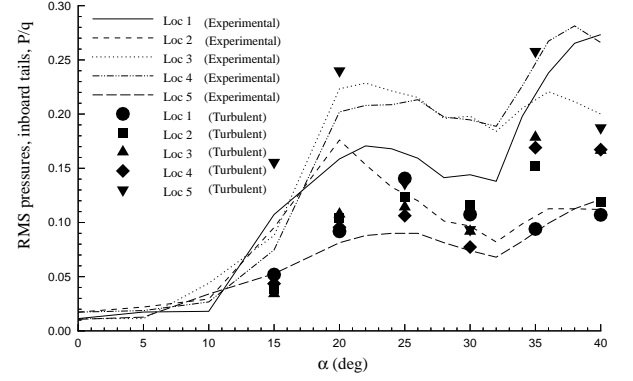


(b) RMS root bending moment

Figure 4: Mean and RMS root bending moment on the flexible tails.

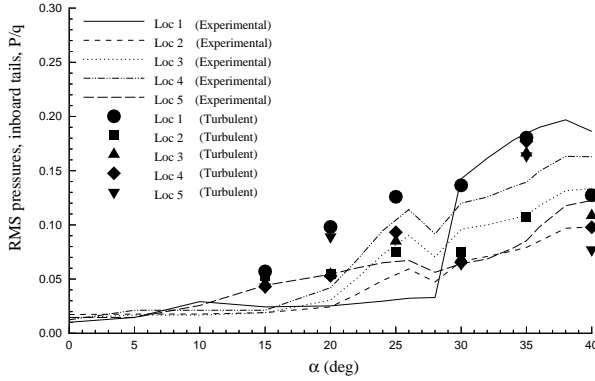


(a) Inner surface

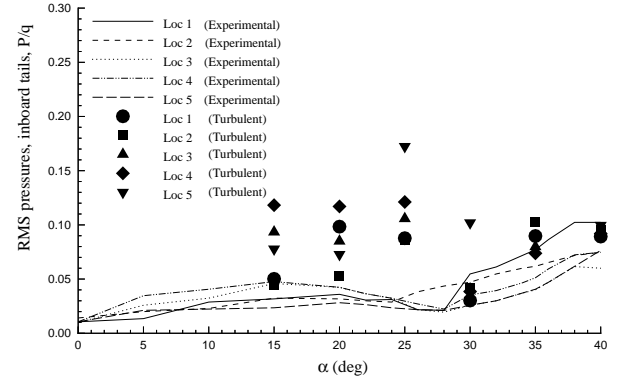


(b) Outer surface

Figure 1: RMS pressures at the specified five locations on the tail, inboard position.

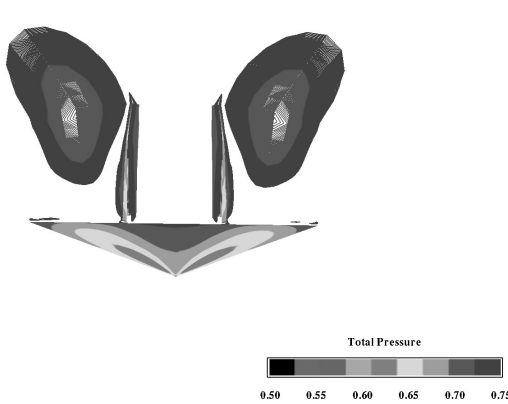


(a) Inner surface

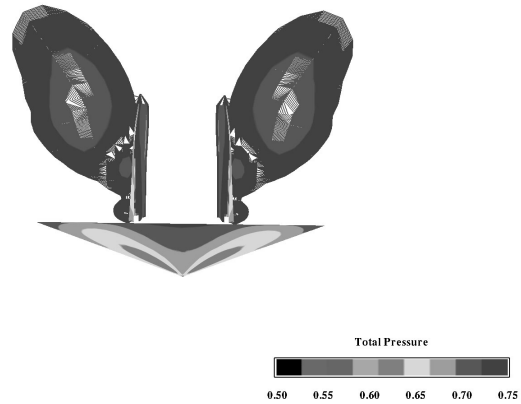


(b) Outer surface

Figure 2: RMS pressures at the specified five locations on the tail, outboard position.

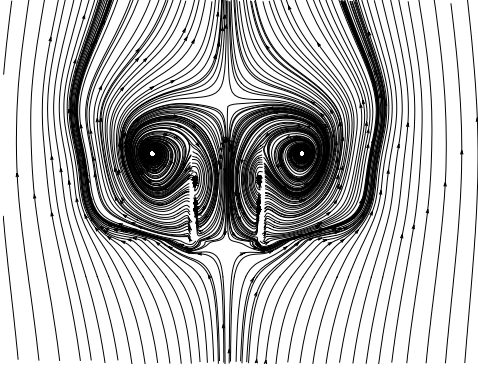


(a) $x = 1.03$

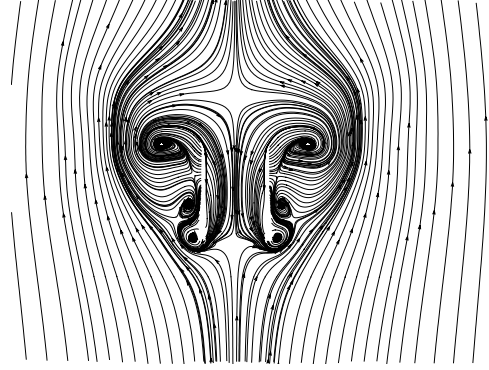


(b) $x = 1.22$

Figure 3: Snap shots of total pressure in a cross-flow planes, (Inboard position). $M_\infty = 0.3$, $\alpha = 25^\circ$, $R_e = 1.25 \times 10^6$.

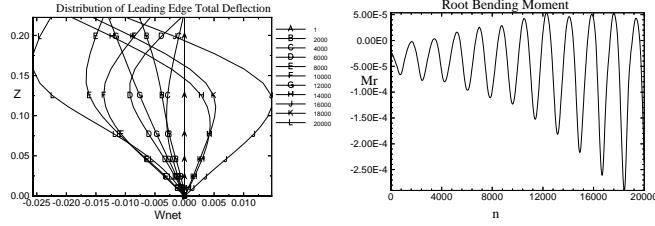


(a) $x = 1.03$

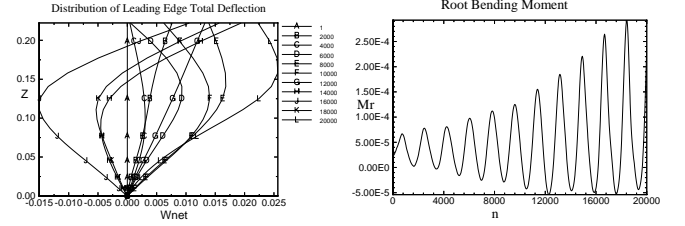


(b) $x = 1.22$

Figure 4: Snap shots of instantaneous streamlines in a cross-flow planes, (Inboard position). $M_\infty = 0.3$, $\alpha = 25^\circ$, $R_e = 1.25 \times 10^6$.

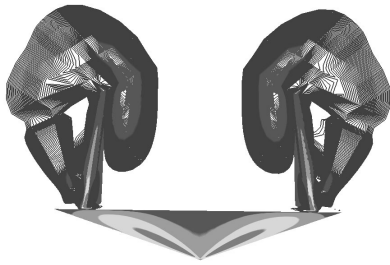


(a) Left tail

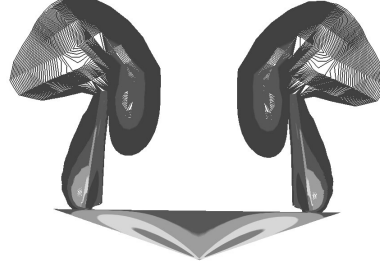


(b) Right tail

Figure 5: Total structural deflections and root bending moment for an uncoupled bending-torsion case. $M_\infty = 0.3$, $\alpha = 25^\circ$, $R_e = 1.25 \times 10^6$, (Inboard position).



(a) $x = 1.03$



(b) $x = 1.22$

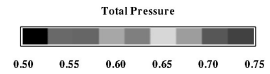
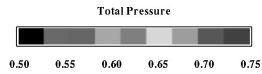
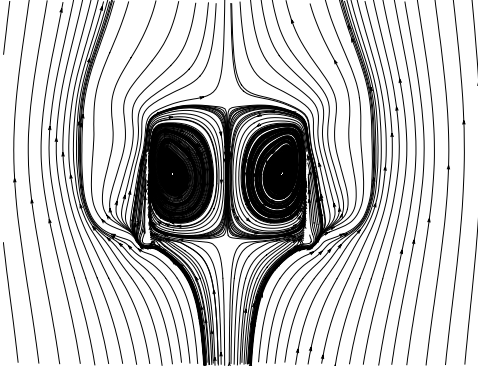
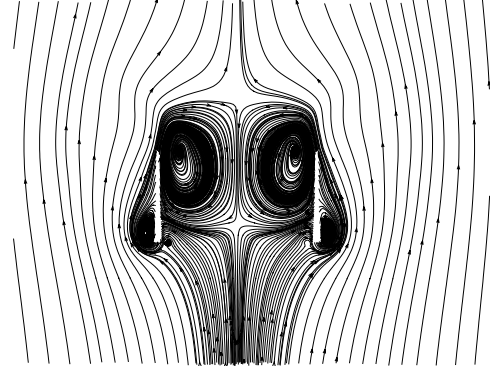


Figure 6: Snap shots of total pressure in a cross-flow planes, (Outboard position). $M_\infty = 0.3$, $\alpha = 25^\circ$, $R_e = 1.25 \times 10^6$.

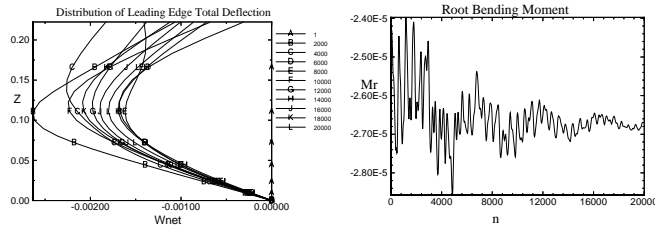


(a) $x = 1.03$

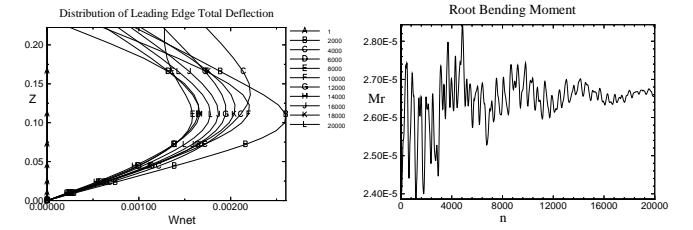


(b) $x = 1.22$

Figure 7: Snap shots of instantaneous streamlines in a cross-flow planes, (Outboard position). $M_\infty = 0.3$, $\alpha = 25^\circ$, $R_e = 1.25 \times 10^6$.

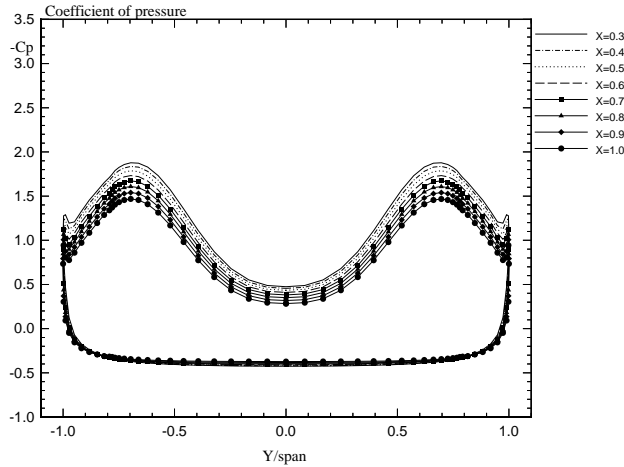


(a) Left tail

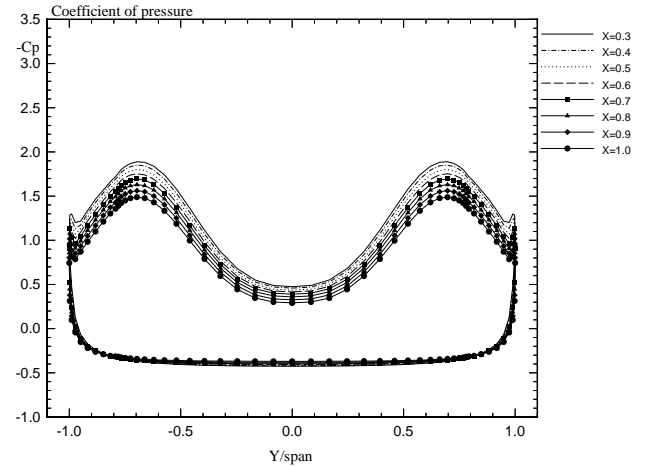


(b) Right tail

Figure 8: Total structural deflections and root bending moment for an uncoupled bending-torsion case. $M_\infty = 0.3$, $\alpha = 25^\circ$, $R_e = 1.25 \times 10^6$, (Outboard position).



(a) Initial conditions



(b) Uncoupled case, after $it = 9,600$

Figure 9: Distribution of Coefficient of pressure. Outboard position, $M_\infty = 0.3$, $\alpha = 25^\circ$, $R_e = 1.25 \times 10^6$.

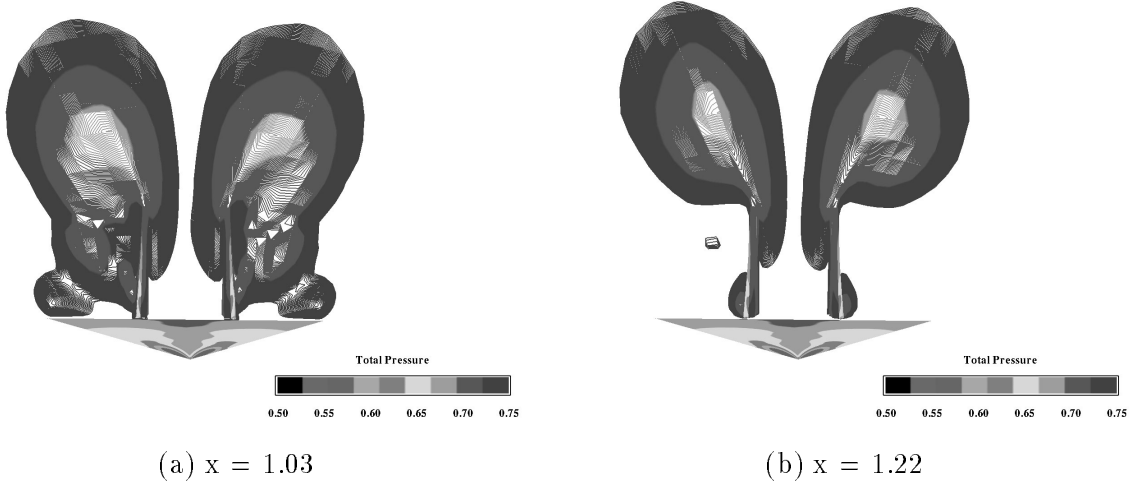


Figure 10: Snap shots of total pressure in a cross-flow planes, (Inboard position). $M_\infty = 0.3$, $\alpha = 40^\circ$, $R_e = 1.25 \times 10^6$.

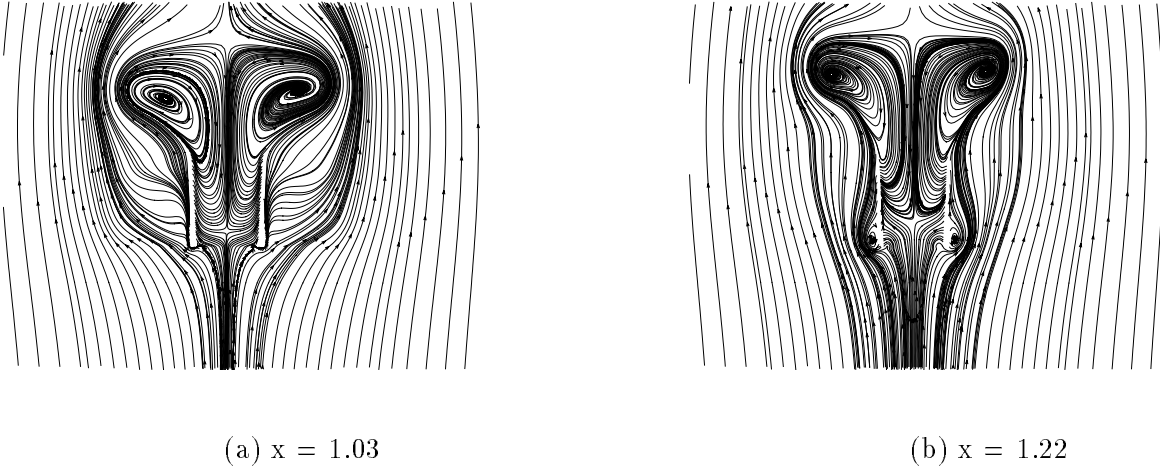


Figure 11: Snap shots of instantaneous streamlines in a cross-flow planes, (Inboard position). $M_\infty = 0.3$, $\alpha = 40^\circ$, $R_e = 1.25 \times 10^6$.

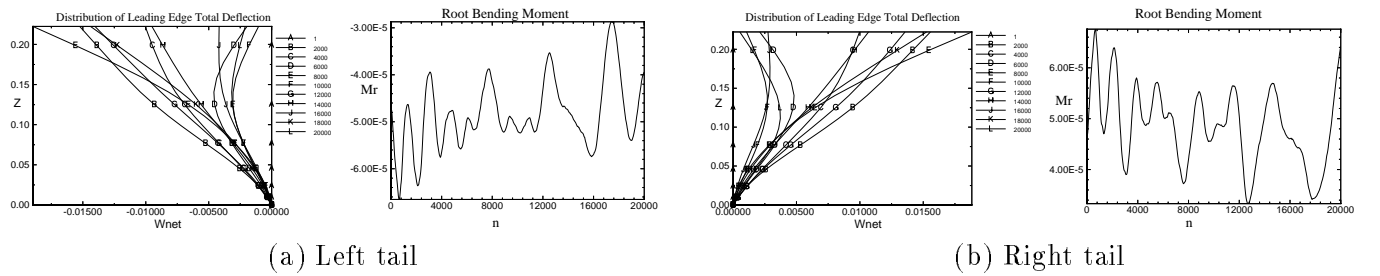
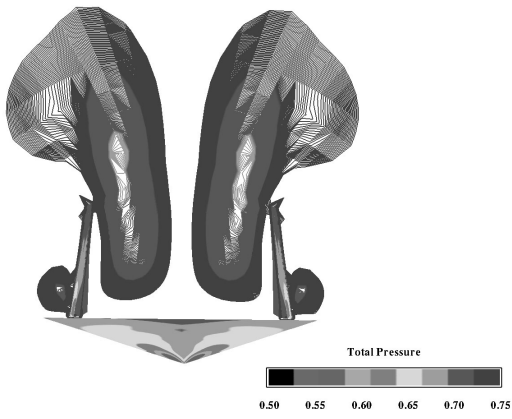
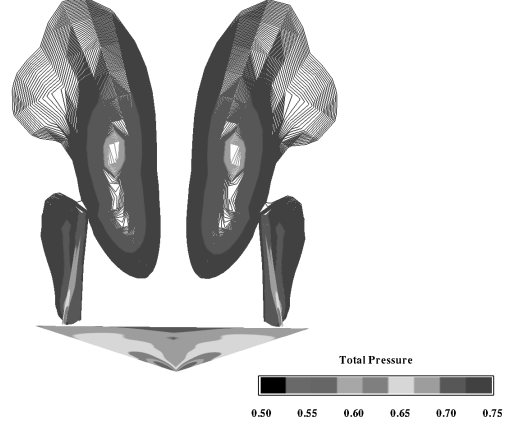


Figure 12: Total structural deflections and root bending moment for an uncoupled bending-torsion case. $M_\infty = 0.3$, $\alpha = 40^\circ$, $R_e = 1.25 \times 10^6$, (Inboard position).

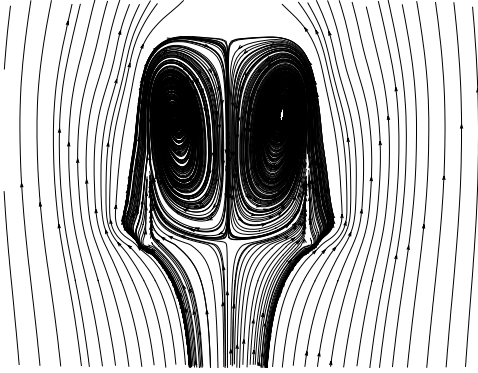


(a) $x = 1.03$

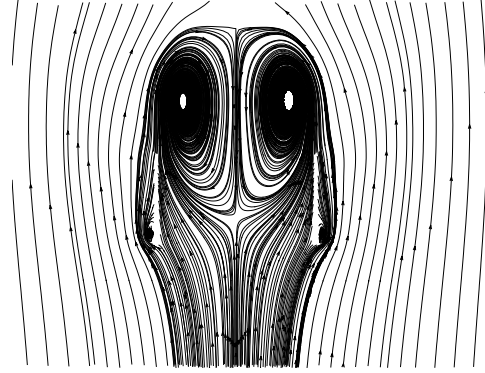


(b) $x = 1.22$

Figure 13: Snap shots of total pressure in a cross-flow planes, (Outboard position). $M_\infty = 0.3$, $\alpha = 40^\circ$, $R_e = 1.25 \times 10^6$.

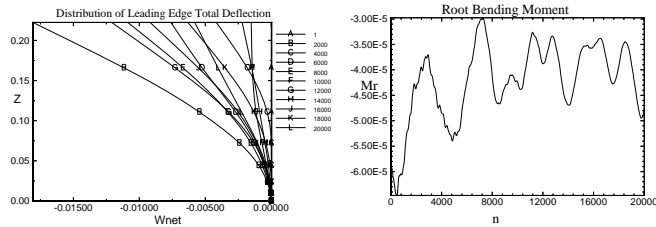


(a) $x = 1.03$

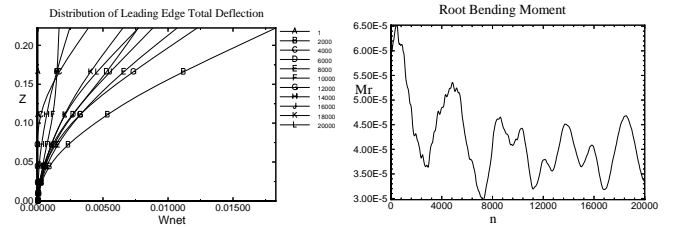


(b) $x = 1.22$

Figure 14: Snap shots of instantaneous streamlines in a cross-flow planes, (Outboard position). $M_\infty = 0.3$, $\alpha = 40^\circ$, $R_e = 1.25 \times 10^6$.

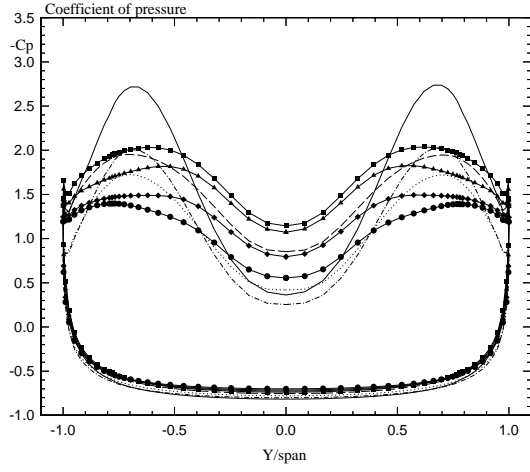


(a) Left tail

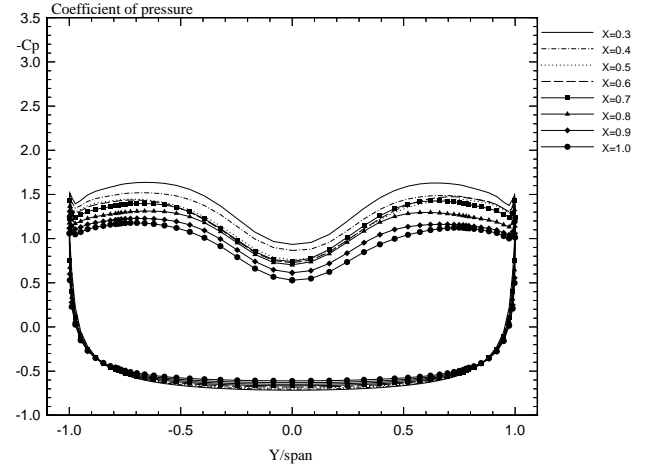


(b) Right tail

Figure 15: Total structural deflections and root bending moment for an uncoupled bending-torsion case. $M_\infty = 0.3$, $\alpha = 40^\circ$, $R_e = 1.25 \times 10^6$, (Outboard position).

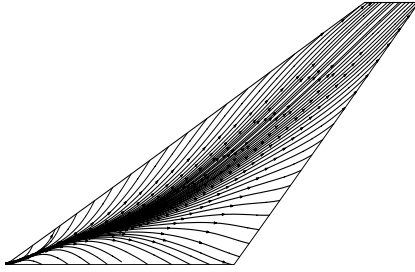


(a) Initial conditions

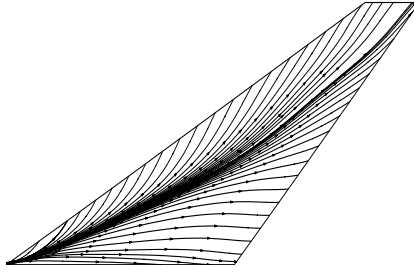


(b) Uncoupled case, after $it = 9,600$

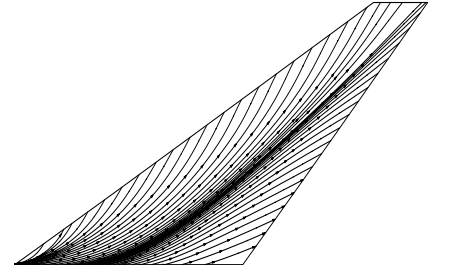
Figure 16: Distribution of Coefficient of pressure. Outboard position, $M_\infty = 0.3$, $\alpha = 40^\circ$, $R_e = 1.25 \times 10^6$.



(a) $\alpha = 20^\circ$

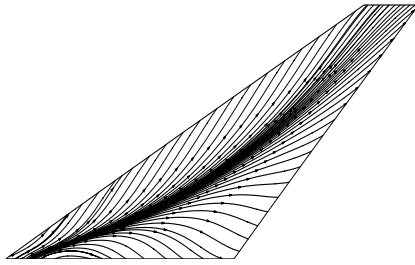


(b) $\alpha = 30^\circ$

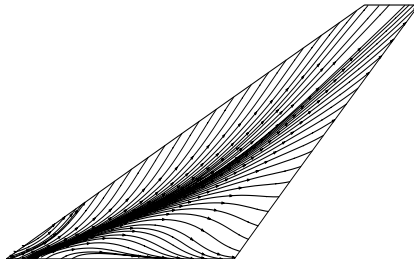


(c) $\alpha = 40^\circ$

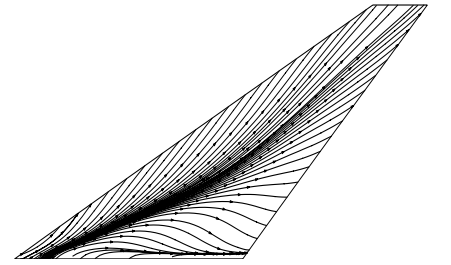
Figure 17: Tail surface flow, inner surface. Uncoupled case after $it = 9,600$, outboard tails.



(a) $\alpha = 20^\circ$



(b) $\alpha = 30^\circ$



(c) $\alpha = 40^\circ$

Figure 18: Tail surface flow, outer surface. Uncoupled case after $it = 9,600$, outboard tails.